Case Studies in Chemical and Environmental Engineering 14 (2026) 101514

Contents lists available at ScienceDirect

Case Studies in Chemical and Environmental Engineering

journal homepage: www.sciencedirect.com/journal/case-studies-in-chemical-and-environmental-engineering

Speciation of chromium in ferrochrome slag via laboratory high-energy-resolution von Hámos X-ray absorption spectroscopy

Jihad El Guettioui [a,b,*], Adél Sarolta Rácz [c], Erzsébet Harman-Tóth [d,e], Tamás G. Weiszburg [d], Zoltán Németh [a]

[a] HUN-REN Wigner Research Centre for Physics, Konkoly Thege M. 29-33, 1121, Budapest, Hungary
[b] Hevesy György PhD School of Chemistry, Eötvös Loránd University, Pázmány P. Sétány 1A, 1117, Budapest, Hungary
[c] HUN-REN Centre for Energy Research, Konkoly Thege M. út 29-33, 1121, Budapest, Hungary
[d] Department of Mineralogy, Eötvös Loránd University, Pázmány P. Sétány 1C, 1117, Budapest, Hungary
[e] Eötvös Museum of Natural History, Eötvös Loránd University, Pázmány P. Sétány 1C, 1117, Budapest, Hungary

ARTICLE INFO

Keywords:
Ferrochrome slag
Chromium speciation
XANES
EXAFS
XPS
LCF

ABSTRACT

During ferrochromium alloy manufacturing, ferrochrome slag is an inevitable industrial residue. Its environmental impacts depend on chromium speciation rather than on total chromium content alone. This study investigates chromium speciation within a low-carbon ferrochrome slag aliquot from a large-scale production facility in the Ural Mountains, using high-energy-resolution laboratory von Hámos X-ray absorption spectroscopy (XAS), a novel technique only recently made accessible for routine characterization, designed to approach synchrotron-level performance. XANES analysis reveals the predominance of the trivalent oxidation state. LCF results indicate Cr occurs mainly in environments similar to $FeCr_2O_4$ (70.2%), Cr(0) (23.4%), and Cr_2O_3 (6.4%). EXAFS analysis shows that the first (Cr-O) and second (Cr-Cr) coordination shells are arranged in a chromite spinel-like Cr(III) structure. XPS findings confirm the predominance of Cr(III) in the slag. Finally, high-energy-resolution laboratory von Hámos XAS enabled the determination of the chromium oxidation state and the local coordination environment even in a poorly defined soil matrix, which parameters define the mobility, reactivity, and potential toxicity of the ferrochrome slag, and promotes this technique as an accessible and economical alternative for toxic metals speciation, with significant implications for the environmental risk classification and the safe reutilization of ferrochrome slag.

1. Introduction

It is well known that ferrochromium (FeCr) is one of the most used ferroalloys in the stainless-steel industry. Approximately 85% of the global ferrochromium production is used as raw materials, which typically contains 10-30% chromium content. The stainless steel is characterized by high resistance to heat, corrosion, oxidation and mechanical strength, these properties are primarily attributed to the chromium content [1,2]. The global ferrochromium production grows steadily annually due to the wide utilization and high demand of stainless steel in various applications. This sustained increase requires larger quantities of chromite ore and generates significant quantities of smelting by-products.

The ferrochromium smelting is an energy-intensive industrial process conducted in a submerged arc furnace at very high temperatures (1750-1800 °C). In this operation, the chromite ore is reduced by carbonaceous reductants, typically metallurgical coke, these carbothermic reactions separate the molten ferrochromium from impurities and produce by-products such as ferrochrome slag at a rate of 1.2-1.5 tons per ton of ferrochromium alloy [3].

The ferrochrome slag serves as a medium for the removal of impurities and absorption of unreduced oxides, enhancing metal yield and forming a fluid layer. The phase separation is facilitated by the significant density difference between molten ferrochromium metal and slag [4], and also affected by the ferrochrome slag's viscosity, which is influenced by temperature, pressure, and the SiO_2/Al_2O_3 content [5].

The chemical composition of ferrochrome slag bulk is mainly rich in metal oxides, silicon dioxide (SiO_2, 27-33 wt%), aluminium oxide (Al_2O_3, 15-25 wt%), magnesium oxide (MgO, 20-35 wt%), in addition to iron chromium compounds (Fe-Cr, 10-15 wt%) [6,7], along with other

* Corresponding author. HUN-REN Wigner Research Centre for Physics, Konkoly Thege M. 29-33, 1121, Budapest, Hungary.
E-mail address: elguettioui.jihad@wigner.hu (J. El Guettioui).

https://doi.org/10.1016/j.cscee.2026.101514
Received 6 July 2026; Received in revised form 8 October 2026; Accepted 24 October 2026
Available online 27 October 2026
2666-0164/© 2026 The Authors. Published by Elsevier Ltd. This is an open access article under the CC BY license (http://creativecommons.org/licenses/by/4.0/).

minor constituents such as calcium and manganese oxides, as well as various trace elements. The ferrochrome slag's chemical composition is highly influenced by the ore variability, fluxes, and process conditions [8].

Cooling rate of the molten ferrochrome slag significantly impacts its crystallinity, rapid water cooling produces amorphous, glassy phases and fine-grained slag, while slower air cooling promotes the growth of larger crystalline phases [9], commonly forsterite ($(Mg, Fe)_2SiO_4$) and spinel $Mg(Al, Cr)_2O_4$ phases [10]. Understanding the crystallization process of the ferrochrome slag is crucial to determining phase formation, which affects its physical properties such as strength, refractoriness, and chromium stability [11].

Chromium can exist in different oxidation states and form compounds with a large variety of coordination geometries, influencing its properties such as toxicity, mobility, and aqueous concentration. Trivalent and hexavalent oxidation states of chromium are the most relevant for environmental considerations [12]. Trivalent chromium (Cr (III)) is relatively stable and less toxic, typically associated with organic matter, however, Cr(III) is rarely oxidized under natural conditions as dissolved oxygen has already been reported to act very slowly and negligibly [13], although the oxidation can occur via manganese oxide (MnO_2), particularly under acidic conditions [14,15].

In contrast, Cr(VI) is highly toxic, soluble, and mobile in the environment, though it can easily be reduced by Fe(II), dissolved sulfides, and organic compounds [16]. Cr(VI) has been classified as a priority pollutant with significant risk to ecosystems and human health, due to its common presence in industrial waste from steelmaking, electroplating, and ferrochromium production [17].

Ferrochrome slags contain 6-12% of residual chromium, mainly as Cr (III), but with a potential for Cr(VI) formation under oxidative conditions [18,19]. Therefore, the presence of different chromium species in ferrochrome slag, combined with the potential of oxidation under specific conditions, has led many researchers to classify it as hazardous industrial waste, making precise characterization of chromium speciation and leaching behavior into soil and groundwater systems essential. Although most fresh slags are stable and meet the European criteria for inert waste [20], the leaching behavior of chromium varies depending on pH, particle size, and time [18].

Given the high volumes of ferrochrome slag produced and stockpiled annually, there is considerable interest in its safe valorization, ranging from the residual chromium recovery from stockpiled refined slags via magnetic separation [21] to their conversion to brick-type construction materials through autoclave carbonization [22], among others. Safe valorization and rigorous environmental assessment of ferrochrome slag are both critically governed by the oxidation state of the residual chromium and its local structural coordination within the ferrochrome slag matrix.

Despite its environmental significance, few studies on chromium speciation in ferrochrome slag have been conducted. Mandina and Mugadza employed selective leaching and UV-Vis spectrophotometry to prove the dominance of Cr(III) and detect trace Cr(VI) in slag dumps in Zimbabwe [23]. Another multi-analytical study [24] revealed that chromium in ferrochrome slag is primarily hosted in spinel phases, often intergrown with silicates and oxides, which prevents the mineral liberation. Previous research on similar materials demonstrated that the chromium speciation in slag systems is significantly influenced by temperature, oxygen partial pressure, and basicity [25,26]. The accurate determination of chromium oxidation states present in ferrochrome slag is further complicated by their coexistence and transformation under varying slag compositions and processing conditions [27], and by the complex chemical and physical environment (such as silicates, metal oxides, well-crystallized solids, and glassy phases).

Conventional analytical methods often lack the high selectivity needed to distinguish coexisting chromium species in complex slag matrices, where chromium coordination environments are heterogeneous and poorly understood. X-ray absorption spectroscopy (XAS) is a preferred element-selective, non-destructive technique for probing the local coordination environment of transition metals in such complex matrices, regardless of their crystalline order [28,29]. Until recently, XAS measurements were largely restricted to synchrotron facilities because of the high photon flux requirements, and limited access to beamtime made routine industrial and environmental applications difficult. Recent advances in laboratory-scale crystal spectrometer design have now made it possible to perform X-ray absorption and emission spectroscopy measurements in standard research laboratories, offering a practical and more accessible alternative for routine sample characterization [30–33].

The present work employs a high-energy-resolution laboratory-based von Hámos X-ray absorption spectrometer, which offers synchrotron-comparable data quality through a cylindrical analyzer crystal and a position sensitive detector in a compact, cost-effective laboratory setup, to determine the oxidation state distribution and local structural coordination of chromium in a low-carbon ferrochrome slag originating from one of the world's largest ferroalloy producers, located in the Ural Mountains, which manufactures high, medium, and low carbon ferrochrome, using electric arc and direct current furnaces, and maintains a dedicated slag processing facility for managing the slag generated during the smelting process. The heterogeneous mineralogy of the ferrochrome slag, along with the possible coexistence of trivalent Cr(III) and hexavalent Cr(VI) chromium species, is taken into consideration throughout the spectral interpretation.

The laboratory-based von Hámos configuration offers sufficient energy resolution to accurately resolve the Cr K-edge position and pre-edge features in the X-ray absorption spectroscopy (XANES) region, which is sensitive to formal oxidation state. At the same time, the extended X-ray absorption fine structure (EXAFS) region provides detailed information about the local coordination environment by identifying the type, number, and distance of neighboring atoms. X-ray photoelectron spectroscopy (XPS) is used as a surface compositional technique to complement the XAS findings. The aim of this work is to demonstrate that advanced chromium speciation can be performed at a laboratory scale without relying on synchrotron access, offering a practical approach for detailed and rapid characterization of ferrochrome slag for environmental risk assessment and safe valorization.

2. Experimental details

2.1. X-ray absorption spectroscopy

- *Sample origin and preparation*

The slag investigated in this study is a low-carbon ferrochrome slag, classified as a stale, self-disintegrating slag, generated before 2019 at one of the largest ferroalloy production facilities in the Ural Mountains, and stockpiled at the slag dump for a long period under atmospheric conditions. *Self-disintegrating slag* refers to slag that spontaneously breaks down into a fine powder during cooling. This behavior is generally associated with the transformation of the crystal form of dicalcium silicate ($\alpha \rightarrow \beta \rightarrow \gamma\text{-}Ca_2SiO_4$), which is accompanied by an increase in crystal lattice volume, and *stale slag* denotes aged, weathered slag after prolonged stockpiling under atmospheric conditions. The analyzed material consisted of a single aliquot collected from this stockpiled slag, and the original sampling data were not documented.

A set of chromium reference compounds was selected to characterize the chromium species present in the ferrochrome slag. Chromium foil from EXAFS Materials (https://www.exafsmaterials.com), as well as $FeCr_2O_4$ (Kremer Pigmente GmbH & Co. KG), Cr_2O_3 (Sigma Aldrich), $Cr_2(SO_4)_3$, K_2CrO_4, and CrO_3 (Sigma Aldrich), together, these standards represent chromium in the Cr(0), Cr(III), and Cr(VI) oxidation states, and encompass a range of coordination environments (oxide, spinel, sulfate, chromate, and anhydride structures).

The XAFSmass program [34] was used to calculate the optimal

sample mass for transmission XAS measurements to achieve an absorption edge step of approximately 1 at the Cr K-edge. Initially, all powdered samples were combined with microcrystalline cellulose, a binder, to obtain a total mixture mass of 100 mg per pellet. The sample masses ranged from 5.2 to 9.7 mg, while the corresponding cellulose masses ranged from 90.3 to 94.8 mg, the sample-to-cellulose ratio varied depending on the chromium compound.

The mixtures were then ground to ensure homogeneity and facilitate pellet formation. The resulting homogeneous powders were pressed into 13 mm diameter pellets using a manual hydraulic pellet press under an applied load of approximately 5-8 tons. The pellets were mounted between two layers of adhesive Kapton tape and placed directly in a fixed position in front of the X-ray source. All measurements were carried out at room temperature.

- ***Laboratory von Hámos Cr K-edge XANES/EXAFS***

X-ray absorption measurements were performed at the HUN-REN Wigner Research Centre for Physics using the laboratory von Hámos X-ray spectrometer described in detail by Németh et al. [31]. Transmission spectra were recorded with a fixed X-ray tube operated at 9 keV and 40 mA, a cylindrical Si (100) analyzer crystal with n = 4 reflection order, and a Dectris Mythen 1K detector set to a 5 keV energy threshold.

XANES spectra were acquired in a fixed von Hámos geometry configuration, resolving pre-edge features and edge-position shifts indicative of distinct chromium oxidation states. EXAFS measurements require a broader energy range (ca. 5950-6550 eV), which was accessed by collecting spectra over a series of successive configurations with progressively decreasing Bragg angles.

The resulting partial datasets were subsequently merged to produce a single continuous EXAFS spectrum. To achieve a sufficient signal-to-noise ratio at the laboratory scale, three to four measurement series were collected for each sample over one to two days of total acquisition time and merged into a single EXAFS spectrum.

All XAS data were processed using the ATHENA program, part of the Demeter software package, including pre-edge subtraction, normalization, and background removal using the Autobk algorithm, from which the EXAFS oscillations were extracted.

- ***Laboratory von Hámos Fe K-edge XANES***

For the iron K-edge XANES measurement, the laboratory von Hámos X-ray spectrometer geometry was defined according to the calculated Bragg angle for the Fe K-edge energy (~7112 eV), employing a Si(531) analyzer crystal. The X-ray tube was run at 11 keV and 40 mA, with the detector threshold energy set to 6.5 keV.

Despite careful optimization of these experimental parameters, the Fe K-edge spectra showed an inadequate signal-to-noise ratio for reliable spectral interpretation, attributable to the inherently low iron concentration in the ferrochrome slag, as subsequently confirmed by XPS.

Complementary Mössbauer spectroscopy was also attempted, but the data quality remained insufficient for any meaningful interpretation. Fe K-edge XANES data are therefore not reported further. These outcomes are fully consistent with the low iron concentration measured by XPS and highlight its utility as a preliminary compositional screening tool.

2.2. X-ray photoelectron spectroscopy

The X-ray photoelectron spectroscopy (XPS) measurement was performed using a Thermo Scientific Escalab Xi + instrument with Al K α X-ray source (1486.6 eV, 650 μm). Depth profiling was conducted by monoatomic argon ion sputtering (0.5 keV, 45° angle of incidence) over a 2 mm area until steady-state concentration was achieved. Survey spectrum was measured in steps of 0.5 eV with 10 ms dwell time per data point, afterwards the following high-resolution spectra of: Si (2p), C (1s), Ca (2p), O (1s), Cr (2p), F (1s), Fe (2p), Mg (1s), and Al (2s) at 20 eV pass energies with 0.1 eV steps and 50 ms dwell time per data point, thirty scans were taken for Cr and Fe to minimize the noise.

Data were processed using ThermoAvantage software. The atomic concentrations were obtained from the peak areas after removing the background by applying the sensitivity factor library (Althermo1). The charging was compensated by setting the C-C/C-H component at 284.8 eV.

3. Results and discussion

3.1. X-ray photoelectron spectroscopy

X-ray photoelectron spectroscopy was employed to determine the elemental composition of the ferrochrome slag aliquot surface and near-surface regions. The survey spectrum of the ferrochrome slag aliquot prior to argon sputtering is presented in Fig. 1, showing the main elements present in the analyzed material, while minor elements were only detected in high-resolution spectra. The atomic compositions obtained before and after argon sputtering are summarized in Table 1, the ferrochrome slag aliquot is predominantly composed of O, Ca, Si, and Mg, with minor contributions from Al, F, Cr, and Fe.

Depth profiling via argon ion sputtering revealed a notable increase in chromium concentration of approximately 28%, confirming that chromium is present in the bulk of the analyzed ferrochrome slag aliquot rather than as surface contamination, while adventitious carbon decreased. The residual carbon signal originates from the sample itself, and the carbon tape used for mounting.

Fig. 2 presents the high-resolution Cr 2p spectra before and after argon sputtering. Chromium exhibits a complex 2p peak structure; Cr (III) possesses unpaired d electrons resulting in characteristic multiplet splitting in the 2p region, whereas Cr(VI), with fully paired d electrons, exhibits a single peak at approximately 579.5 eV, as cited in the literature data. The quantification of Cr(VI) is complicated by the spectral overlap with the Cr(III) multiplet, which elevates the detection limit for Cr(VI) to approximately 10% of total chromium in a Cr(III) dominated matrix, any contribution below this value is considered undetectable [35].

The XPS results confirm the presence of Cr, Fe, and other key elements. The absence of a significant peak at 579.5 eV suggests that chromium is predominantly present as Cr(III) in the analyzed ferrochrome slag aliquot.

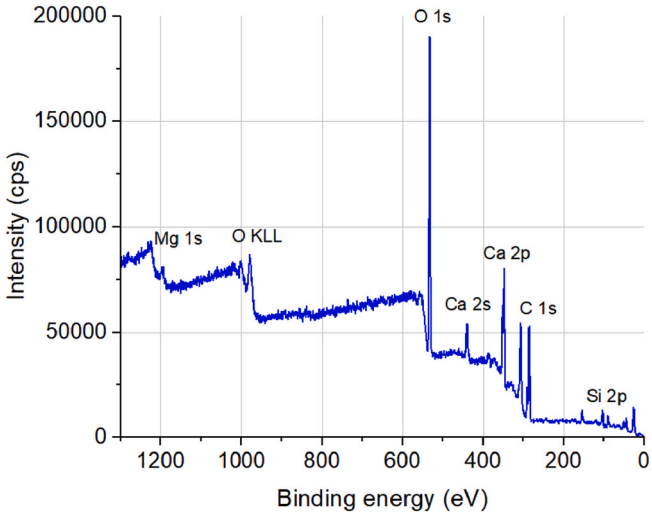


Fig. 1. XPS survey spectrum of Cr-rich slag aliquot before monoatomic argon sputtering.

Table 1
Elemental composition of the ferrochrome slag aliquot surface before and after monoatomic argon sputtering (atomic %).

Elements	O	Mg	Al	Ca	Si	Cr	Fe	F	C
Surface (at. %)	42.1	2.8	1.5	9.0	6.8	**0.68**	0.38	1.6	35.2
After Sputtering, steady state concentration (at. %)	46.2	6.2	2.0	14.7	10.2	**0.94**	0.45	1.5	17.8

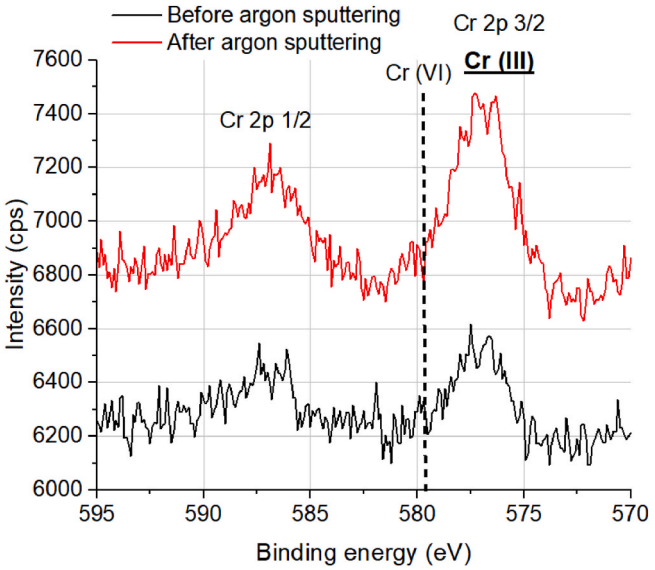


Fig. 2. High-resolution Cr 2p XPS spectra from the surface and after monoatomic argon sputtering.

3.2. Chromium K-edge XANES

- ***Oxidation state determination***

Normalized Cr K-edge XANES spectra of the analyzed ferrochrome slag aliquot and all six reference compounds (Cr(0), Cr(III), Cr(VI)) are presented in Fig. 3a, together with their first derivative spectra in Fig. 3b. All Cr(III) reference materials ($FeCr_2O_4$, Cr_2O_3, $Cr_2(SO_4)_3$) exhibit their absorption edges at lower energies, whereas the two Cr(VI) standards (K_2CrO_4, CrO_3) display a noticeable high-energy edge shift of approximately 4-6 eV. This energy shift reflects the increase in core-electron binding energy associated with the reduced electron density at higher oxidation states [36].

In addition to the absorption edge energy shift, tetrahedrally coordinated Cr(VI) compounds typically display a characteristic pre-edge peak at ~5992 eV, arising mainly from a 1s→3d transition that gains significant electric-dipole intensity through 3d–4p orbital hybridization, permitted by the absence of an inversion centre in non-centrosymmetric tetrahedral environments. Octahedrally coordinated Cr(III) species, by contrast, show a much weaker pre-edge feature, as the centrosymmetric ligand field forbids electric-dipole 1s→3d transitions, leaving only a weak quadrupole allowed contribution [37,38]. The distinct pre-edge peak serves as a robust spectral fingerprint for distinguishing Cr(III) from Cr(VI).

The XANES spectrum of the ferrochrome slag aliquot (red) closely resembles the Cr(III) standard spectra, with an absorption edge position

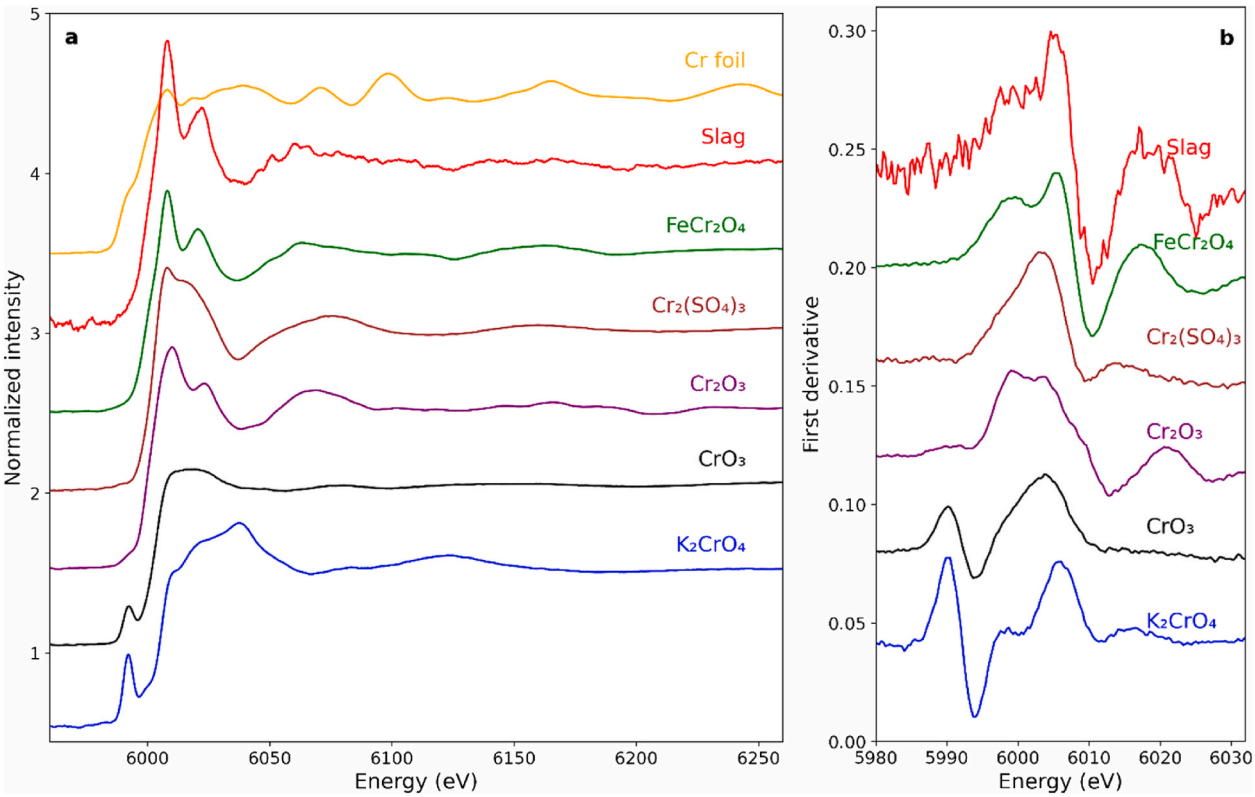


Fig. 3. Normalized Cr K-edge XANES spectra (a) and their first derivatives (b) of the ferrochrome slag aliquot and reference materials: Cr(0): Cr foil, Cr(III): $FeCr_2O_4$, Cr_2O_3, $Cr_2(SO_4)_3$, Cr(VI): K_2CrO_4, CrO_3.

that lies in the lower energy range of Cr(III). The absence of the pronounced characteristic pre-edge peak of Cr(VI) indicates that chromium in the analyzed aliquot is predominantly present as Cr(III). This is supported by the first-derivative spectra (Fig. 3b), in which the slag aliquot shows derivative features that align with those of Cr(III) references, both in peak position and overall shape.

In particular, the first derivative maximum at 5997.5 eV, followed by the main edge peak at ~6004 eV, mirrors the Cr(III) spectral pattern and remains well below the Cr(VI) derivative peaks. The absence of any high-energy Cr(VI) type derivative maximum further confirms that no detectable Cr(VI) is present in the analyzed slag aliquot within the detection limit given below, and indicates that chromium occurs almost entirely as Cr(III) in an environment consistent with octahedral coordination.

Based on the noise level of the pre-edge baseline in the ferrochrome slag aliquot spectrum relative to the pre-edge peak intensity of the Cr (VI) K_2CrO_4 reference measured in the same laboratory von Hámos XANES setup, the detection limit for Cr(VI) was estimated at approximately 5.7% of total chromium. This is consistent with the detection limit reported for synchrotron-based Cr K-edge XANES in the literature, approximately 5% of the total chromium [39].

- ***Linear Combination Fitting (LCF)***

The linear combination fitting (LCF) method was applied using the ATHENA software package [40] to quantitatively determine the proportions of chromium species present in the ferrochrome slag by reconstructing the experimental XANES spectrum as a weighted linear superposition of known reference spectra from known standards. The LCF analysis was carried out over an energy range of −30 to 50 eV relative to the absorption edge, using six reference compounds, Cr foil, $FeCr_2O_4$, Cr_2O_3, $Cr_2(SO_4)_3$, K_2CrO_4, and CrO_3 as standards. All twenty-six combinatorial fits of these standards were evaluated to identify the most suitable combination, this selection is based on the R-factor parameter, which quantifies the goodness of fit. The optimal linear combination fit, shown in Fig. 4, was obtained using a three component combination of Cr-foil, $FeCr_2O_4$, and Cr_2O_3, yielding an R-factor of 0.002. The results are model-dependent, and they reflect the chosen reference set along with the fitting constraints, and they do not constitute an independent identification of mineral phases.

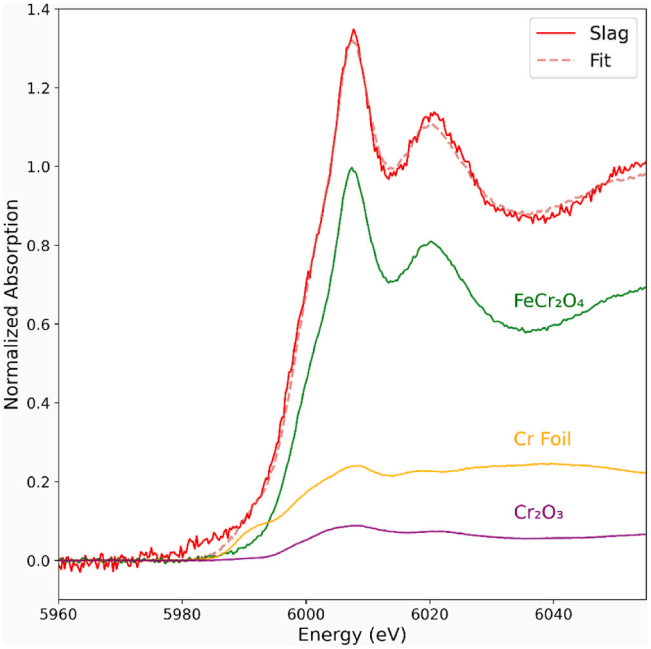


Fig. 4. Linear combination fitting of the ferrochrome slag XANES data using Cr foil, $FeCr_2O_4$, and Cr_2O_3 standards.

The application of the LCF to experimental XANES data reveals that the fitted contributions were 70.2% (±1.9) $FeCr_2O_4$-like, 23.4% (±0.8) Cr(0)-like, and 6.4% (±4.8) Cr_2O_3-like environments. It should be noted that, with the use of chromium foil as a reference, the Cr(0)-like contribution should not be interpreted as evidence for the presence of pure metallic chromium. Still, this contribution most likely represents chromium in a metallic or metal-rich environment, such as residual Fe-Cr alloy droplets entrained in the ferrochrome slag.

The fitted results indicate that the two Cr(III)-like components together account for 76.6%, and the Cr(0)-like component for 23.4% likely originating from Fe-Cr alloy, which aligns perfectly with the reducing smelting conditions under which ferrochrome slag is formed. Within this model, the relatively small uncertainties associated with the $FeCr_2O_4$-like and Cr(0)-like components (±1.9% and ±0.8%) indicate that these contributions are robust and consistently required to reproduce the experimental spectrum. In contrast, the larger uncertainty associated with the Cr_2O_3-like component (±4.8%) suggests that this minor component is less precisely constrained. Importantly, this uncertainty does not alter the overall interpretation of the spectrum.

During the LCF application, no hexavalent chromium standards were required to obtain a satisfactory fit, corroborating the absence of any detectable Cr(VI) above the detection limit established by both XANES edge analysis and XPS results described in previous sections. This applies only to the analyzed aliquot and not to the stockpile in general. The coexistence of chromite, chromium oxide, and metallic chromium Cr(0)-like environments identified here is consistent with synchrotron-based chromium speciation studies of analogous high-temperature residues, although these studies concern other materials and do not validate the present results [41]. demonstrated that during the direct reduction of chromite, chromium is progressively dissolved into slag, then reduced in the molten phase, and finally metallized, producing mixed spinel-, oxide-, and metal-bearing environments in which Cr(III), Cr(II), and Cr (0) coexist within the final product. Their findings are compatible with the interpretation of the present data as reflecting a heterogeneous, partially reduced chromite derived system. Similarly, another synchrotron-based XANES study [42] showed that chromium in thermally processed mineral residues is commonly stabilized in spinel-like and Cr-silicate environments, and that chromium speciation is strongly controlled by the local redox environment and melt interactions during high-temperature processing.

However, the quantitative Cr(0)-like fraction should be interpreted with caution, as the reference spectrum used for this component was obtained from pure chromium foil, whereas chromium in the slag is more likely to exist in an Fe-Cr alloy. The local coordination and electronic structure of chromium in an Fe-Cr alloy may differ from those of pure metallic chromium, which may introduce a systematic bias in the fitted Cr(0)-like contribution. No suitable Fe-Cr alloy reference standard was available for the presented measurements, and the Cr foil was used as the closest available spectral equivalent. The reported value (23.4 ± 0.8%) should therefore be considered as the contribution of the spectrum exhibiting a Cr(0)-like metallic character rather than as an exact concentration of pure metallic chromium.

The simultaneous presence of spinel-like, Cr(0)-like, and chromium oxide-like spectral contributions in the present ferrochrome slag aliquot is not anomalous but rather a characteristic feature of ferrochrome slag produced under industrial smelting conditions. This mixed-valence chromium distribution reflects incomplete thermodynamic equilibration and heterogeneous redistribution of chromium during ferrochrome production, rather than the formation of a single homogeneous chromium phase. Because sampling information is unavailable, this interpretation cannot be generalized beyond the analyzed aliquot.

3.3. Local coordination environment by EXAFS analysis

To investigate the local atomic environment around chromium atoms in the ferrochrome slag aliquot, the extended X-ray absorption fine structure (EXAFS) data were processed using the ATHENA program. The Fourier transform (FT) of the EXAFS spectra was applied over the k-range 3-11 $Å^{-1}$, using a k^2 weighting factor and a Hanning window for the ferrochrome slag aliquot and Cr (III). Fig. 5 presents the Fourier transform (FT) magnitude in R-space and the corresponding k^2-weighted χ(k) EXAFS spectra for the ferrochrome slag aliquot and Cr (III) references $FeCr_2O_4$, Cr_2O_3, and $Cr_2(SO_4)_3$.

In k-space (Fig. 5b), the EXAFS oscillation patterns of the ferrochrome slag aliquot resemble those of iron chromite ($FeCr_2O_4$) and chromium oxide (Cr_2O_3). This high degree of similarity in frequency suggests that the local atomic arrangement around Cr(III) in the ferrochrome slag aliquot is analogous to that found in spinel-type and corundum-type structure environments, with a slight difference between them due to the height of the outer peaks. In R-space (Fig. 5a), all samples display a dominant peak at approximately ~1.6 Å (without phase correction), corresponding to the first Cr–O coordination shell. This feature reflects the octahedral environment characteristic of trivalent chromium coordinated by oxygen atoms. A second shell peak is observed at 2-3 Å for $FeCr_2O_4$ and Cr_2O_3, attributed to Cr–Cr and Cr–Fe scattering paths, reflecting a well-ordered metal-metal coordination environment in these crystalline oxide phases.

The ferrochrome slag aliquot shows a similar second-shell feature, which is consistent with Cr octahedrally coordinated within a crystalline oxide matrix with a defined metal-metal coordination. Conversely, $Cr_2(SO_4)_3$ lacks a distinct second-shell peak, consistent with the molecular coordination environment created by sulfate ligands that isolate Cr ions and eliminate Cr–Cr interactions. The qualitative similarity of the ferrochrome slag FT to those of $FeCr_2O_4$ standards in both first- and second-shell peak positions indicates that the chromium in the slag aliquot occurs predominantly as octahedrally coordinated Cr (III).

Qualitative comparison of the experimental FT of the ferrochrome slag aliquot with theoretical scattering paths from both $FeCr_2O_4$ and Cr_2O_3 structural models is presented in Fig. 6. Theoretical scattering paths were generated by FEFF6 calculations (ARTEMIS [40]) based on structural models retrieved from the Crystallography Open Database (COD) [43].

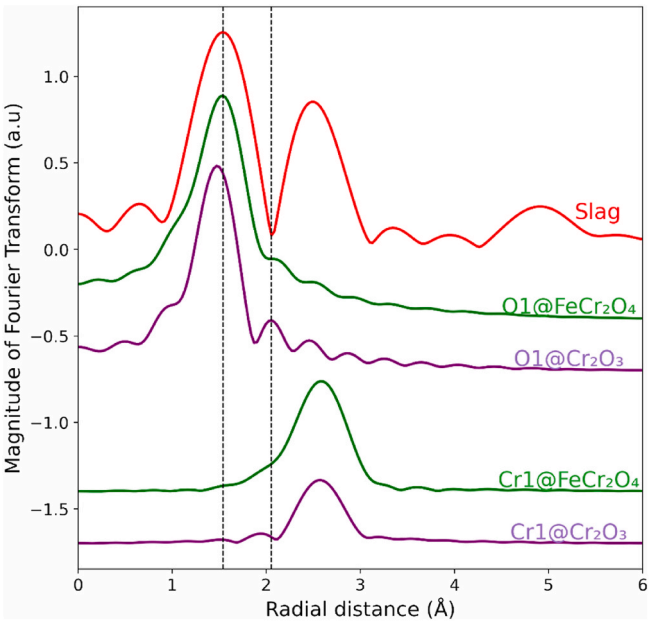


Fig. 6. Comparison of the Fourier Transform of the ferrochrome slag aliquot and the theoretical paths corresponding to the first and second shells of $FeCr_2O_4$ and Cr_2O_3.

Table 2 summarizes the crystal system and space group of the model compounds used in this study, and the theoretical contributions of the first- and second-shell atoms and paths of the standards used, with their theoretical coordination numbers (CN_{th}) and the theoretical bond distances (Reff). Only atoms with distances smaller than 4 Å are shown. The Cr1–O1 and Cr1–Cr1 scattering paths of $FeCr_2O_4$ align well with the first two peaks in the experimental FT. Although the Cr1–O1 and Cr1–Cr1 paths of Cr_2O_3 exhibit structural similarity.

Fig. 6 compares the Fourier Transform of the experimental data of the ferrochrome slag aliquot with selected individual theoretical scattering paths from the $FeCr_2O_4$ and Cr_2O_3 structures, as the FT of the

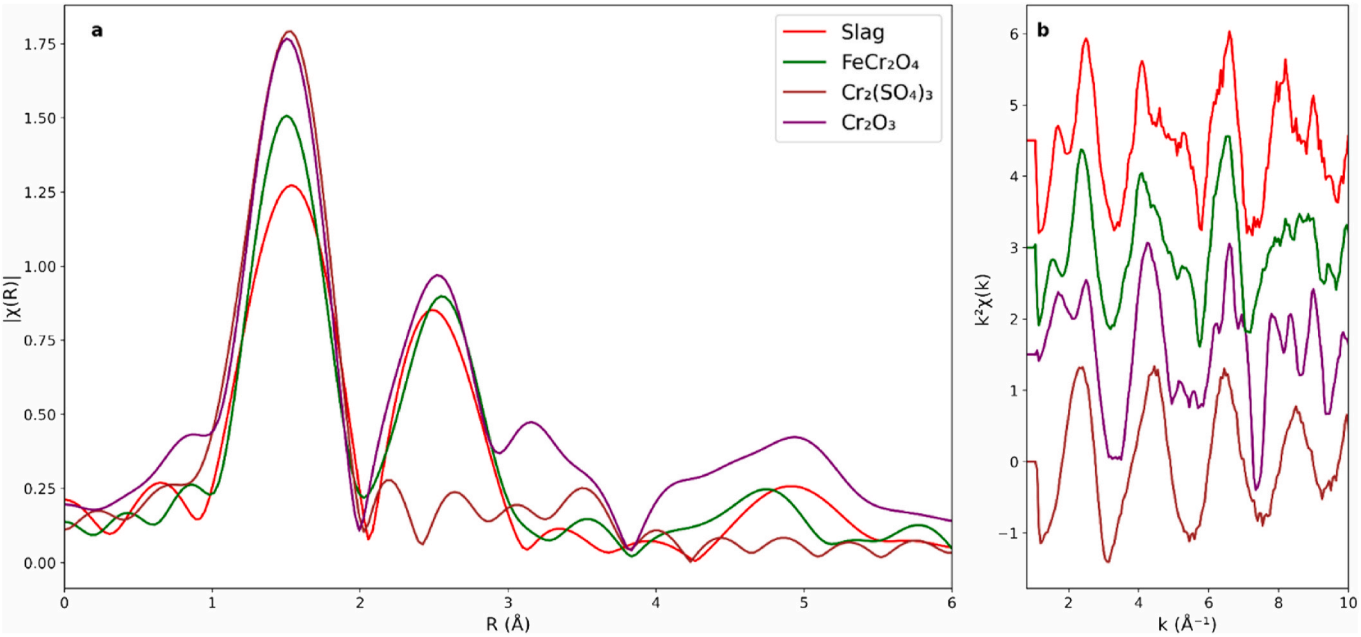


Fig. 5. Fourier Transform (FT) of EXAFS spectra at the Cr K-edge in R-space (a) and the corresponding k^2-weighted spectra in k-space (b) of the slag aliquot and Cr (III): $FeCr_2O_4$, Cr_2O_3, $Cr_2(SO_4)_3$ reference compounds.

Table 2
Crystal and theoretical structural parameters for multiple scattering paths of the model samples, obtained from the Crystallography Open Database (COD) and from the FEFF6 calculations at Cr K-edge using the ARTEMIS program [40].

Samples	Crystal system/space group	Atoms	Paths	CN_{th}	R_{eff} (Å)
$FeCr_2O_4$	Cubic/Fd-3m	O1	Cr1–O1	6	1.994
		Cr1	Cr1–Cr1	6	2.962
		O2	Cr1–O2	2	3.444
		Fe1	Cr1–Fe1	6	3.473
Cr_2O_3	Trigonal/R -3c	O1	Cr1–O1	3	1.905
		Cr1	Cr1–Cr1	1	2.767
		Cr2	Cr1–Cr2	3	2.906

aliquot is best characterized at distances shorter than 3 Å. Only scattering paths with lengths up to 2.9 Å were included in the analysis. As shown in Fig. 6, the Cr1–O1 (Reff = 1.994 Å) and Cr1–Cr1 (Reff = 2.962 Å) scattering paths of $FeCr_2O_4$ align perfectly with the first two peaks observed in the experimental Fourier Transform of the ferrochrome slag aliquot. Although the Cr1–O1 and Cr1–Cr1 paths of Cr_2O_3 also show significant similarity, considering the weight percentage obtained from the linear combination fitting LCF (70.2% $FeCr_2O_4$-like and 6.4% Cr_2O_3-like), which are model-dependent, suggests that $FeCr_2O_4$ as structurally dominant contribution, making it the most appropriate reference model for the EXAFS fitting of the ferrochrome slag aliquot. The experimental data of the $FeCr_2O_4$ standard were also fitted for comparison. Table 3 lists the fitted results.

Quantitative EXAFS fitting was performed in ARTEMIS [40] over the R-range 1–3 Å, using the first two shells (Cr1–O1 and Cr1–Cr1) of the $FeCr_2O_4$ structural model, with amplitude reduction factor (S_0) fixed at 0.7 throughout EXAFS fitting, consistent with the literature value for chromium K-edge analysis. Table 3 lists the fitted structural parameters for both the $FeCr_2O_4$ reference compound and the ferrochrome slag aliquot, and the corresponding experimental and fitted FT spectra are shown in Fig. 7.

For the EXAFS fit for the $FeCr_2O_4$ reference, the fitted Cr1–O1 bond distance of 1.975 Å (CN = 5.62) and Cr1–Cr1 with a bond distance of 2.987 Å (CN = 5.84) are in excellent agreement with the crystallographic values for cubic chromite spinel (Reff(Cr1–O1) = 1.994 Å and Reff(Cr1–Cr1) = 2.979 Å, Table 2), with a low R-factor of 0.007 confirming a high quality fit.

For the ferrochrome slag aliquot, the fitted Cr1–O1 and Cr1–Cr1 bond distances are 1.961 Å and 2.979 Å, respectively, with coordination numbers of 5.10 and 6.54 (R-factor = 0.04). The Cr1–O1 bond distance is slightly shorter than the $FeCr_2O_4$ reference value (by ~0.014 Å), and the first-shell coordination number is nominally reduced relative to the theoretical value of 6 (Table 2), both indicative of an approximately octahedral, structurally disordered spinel-like Cr(III) environment, in line with possible structural disorder in the heterogeneous slag matrix composed of intergrown crystalline and potentially glassy phases. The higher R-factor (0.04 vs 0.007) is expected for such a complex material and reflects inherent structural heterogeneity, this value falls within the range generally considered acceptable for EXAFS fitting of complex industrial matrices.

The larger Debye-Waller factor for the first shell of the ferrochrome slag aliquot (σ^2 = 0.0063 vs. 0.0039 $Å^2$ for the standard) is consistent

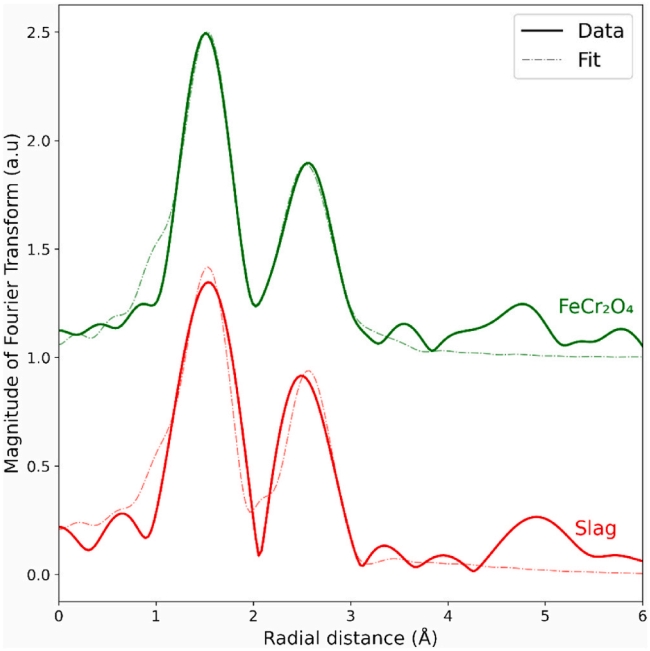


Fig. 7. Best fitting of the FT of the experimental data of ferrochrome slag aliquot and $FeCr_2O_4$, and the theoretical data.

with greater structural disorder around Cr atoms in the ferrochrome slag aliquot [29,44]. The second shell Cr1–Cr1 distance (2.979 Å) agrees with the $FeCr_2O_4$ theoretical value (2.962 Å) and with distances expected for edge-sharing CrO_6 octahedra in the spinel structure [10,24]. The elevated energy shift (ΔE) for the slag (+8.19 eV) compared to the reference (−2.79 eV) is within the normal range for complex multi-phase materials where multiple chromium environments contribute to the edge region and may reflect the multiple Cr(III) environments, as suggested previously by LCF.

During the fitting process, several attempts were made to include additional scattering paths, Cr1–O2 and Cr1–Fe1, in the model. Although these paths yielded an acceptable fit, but the resulting parameters, particularly the bond distances R ± ΔR (Å), fell outside physically reasonable ranges, even when the coordination numbers were held fixed. These paths were therefore excluded from the final fit.

It is also worth noting that, although the LCF and k-space analysis results strongly suggest $FeCr_2O_4$ as the most suitable structural reference, the theoretical scattering paths derived from the Cr_2O_3 structural model were also evaluated. This yielded a significantly poor fit with unreasonable structural parameters, and these results are therefore not reported.

The combined XANES and EXAFS analysis mutually and unambiguously proves that chromium in the ferrochrome slag aliquot is predominantly present as Cr(III), adopting a chromite spinel-like arrangement in which oxygen atoms form the first shell and chromium atoms constitute the second shell in an approximately octahedral, structurally disordered geometry. This arrangement with the chromium firmly incorporated within the thermodynamically stable spinel lattice is

Table 3
The fitted structural parameters of ferrochrome slag aliquot and $FeCr_2O_4$, obtained from EXAFS fitting at Cr K-edge using the $FeCr_2O_4$ theoretical model cited in Table 2. CN stands for the coordination number, R for the bond distance. The Debye-Waller factor σ^2 and the energy shift ΔE. S_0 parameter was fixed at 0.7. The values in parentheses represent the standard errors of the fitted parameters, as calculated by the Artemis EXAFS-fitting software.

Samples	Paths	CN	R(Å)	$\sigma^2(Å^2)$	ΔE(eV)	S_0	R_{factor}
$FeCr_2O_4$	Cr1–O1	5.62 (0.41)	1.975 (0.019)	0.00391 (0.0009)	−2.79 (1.08)	0.7 (fixed)	0.007
	Cr1–Cr1	5.84 (1.05)	2.987 (0.025)	0.00146 (0.0019)			
Ferrochrome slag aliquot	Cr1–O1	5.10 (1.20)	1.961 (0.033)	0.00626 (0.0034)	8.191 (1.89)	0.7 (fixed)	0.04
	Cr1–Cr1	6.54 (3.42)	2.979 (0.017)	0.01364 (0.0064)			

expected to influence its environmental behavior; however, evaluating the actual leaching risk and environmental safety of the ferrochrome slag would require dedicated leaching studies that also account for factors such as particle size, pH, coexisting oxidants, and long-term weathering.

4. Conclusion

This study demonstrates the effectiveness of laboratory-based high-energy-resolution von Hámos X-ray absorption spectroscopy (XAS) for chromium speciation in an aliquot of aged ferrochrome slag, a complex industrial matrix with notable environmental and health concerns. The combined XANES analysis and linear combination fitting indicate that chromium in the analyzed aliquot is predominantly Cr(III), accounting for 76.6% of total chromium and no detectable Cr(VI) above the detection limit. The EXAFS fitting analysis confirmed the octahedral coordination of Cr(III) within a slightly structurally disordered chromite spinel-like environment. At the same time, XPS independently corroborated the predominance of Cr(III) at the surface. The dominance and stabilization of chromium within a spinel lattice suggest a potentially reduced propensity for Cr(VI) leaching under ambient conditions; however, confirming its environmental safety would require dedicated leaching studies.

Sampling data for the analyzed slag aliquot are unavailable. The findings, including the absence of detectable Cr(VI), therefore apply only to this aliquot and cannot be generalized to the stockpile or to ferrochrome slag in general. This speciation study thus provides a scientific basis for future investigations of Cr leaching behavior and associated environmental risk on representative sample material. Within these limits, laboratory von Hámos X-ray absorption spectroscopy delivers high-quality bulk speciation data, positioning it as a promising, accessible, and cost-effective alternative tool to synchrotron-based measurements for the routine environmental characterization of toxic metal-bearing industrial wastes.

CRediT authorship contribution statement

Jihad El Guettioui: Writing – original draft, Methodology, Investigation, Formal analysis. **Adél Sarolta Rácz:** Writing – review & editing, Validation, Investigation. **Erzsébet Harman-Tóth:** Writing – review & editing. **Tamás G. Weiszburg:** Writing – review & editing. **Zoltán Németh:** Writing – review & editing, Validation, Conceptualization.

Declaration of competing interest

The authors declare that they have no known competing financial interests or personal relationships that could have appeared to influence the work reported in this paper.

References

[1] Pierre-Jean Cunat, Alloying Elements in Stainless Steel and Other Chromium-Containing Alloys, 2004. January 1.

[2] Preez Du, P. Stephanus, P. M. Van Kaam Tristan, Eli Ringdalen, et al., An overview of currently applied ferrochrome production processes and their waste management practices, Minerals 13 (6) (2023) 809, https://doi.org/10.3390/min13060809.

[3] Shaswat Kumar Das, Ankit Kumar Tripathi, Sapan Kumar Kandi, Syed Mohammed Mustakim, Bhagyadhar Bhoi, Priyanka Rajput, Ferrochrome slag: a critical review of its properties, environmental issues and sustainable utilization, J. Environ. Manag. 326 (January) (2023) 116674, https://doi.org/10.1016/j.jenvman.2022.116674.

[4] Nilamadhaba Sahu, Arijit Biswas, Gajanan U. Kapure, A short review on utilisation of ferrochromium slag, mineral processing and extractive metallurgy review, Miner. Process. Extr. Metall. Rev. 37 (4) (2016) 211–219, https://doi.org/10.1080/08827508.2016.1168415.

[5] Pekka Niemelä, Mauri Kauppi, Production, characteristics and use of ferrochromium slags. Proceedings of the 11th International Ferro-Alloys Congress, 2007. Paper presented at INFACON XI.

[6] L. Holappa, Y. Xiao, Slags in Ferroalloys Production—Review of Present Knowledge, 104, The Journal of The South African Institute of Mining and Metallurgy, 2004, pp. 429–437.

[7] O. Privalov, Ye Abdulabekov, Zh Nurmukhanbetov, M. Kospanov, Zh Mussabekov, Adjustment of high carbon ferrochrome composition in DC furnaces. Paper Presented at Infacon XIII. Proceedings of the 13th International Ferroalloys Congress (Infacon XIII), 2013. June 9.

[8] Merete Tangstad, Johan Paul Beukes, Joalet Steenkamp, Eli Ringdalen, Coal-based reducing agents in ferroalloys and silicon production, in: New Trends in Coal Conversion, Elsevier, 2019, https://doi.org/10.1016/B978-0-08-102201-6.00014-5.

[9] Bin Ding, Qiang Liao, Xun Zhu, Hong Wang, Deep insight into phase transition and crystallization of high temperature molten slag during cooling: a review, Appl. Therm. Eng. 184 (February) (2021) 116260, https://doi.org/10.1016/j.applthermaleng.2020.116260.

[10] Batna Anantha Venkata Ram Kumar, Lakshmi Keshav, Panneerselvam Arul Sivanantham, et al., Comprehensive characterization of ferrochrome slag and ferrochrome ash as sustainable materials in construction, J. Nanomater. 2022 (1) (2022) 8571055, https://doi.org/10.1155/2022/8571055.

[11] P.C. Hayes, Aspects of SAF smelting of Ferrochrome. Tenth International Ferroalloys Congress; INFACON X, 'Transformation through Technology', Cape Town, South Africa, 2004. February 1.

[12] Rumpa Saha, Rumki Nandi, Bidyut Saha, Sources and toxicity of hexavalent chromium, J. Coord. Chem. 64 (10) (2011) 1782–1806, https://doi.org/10.1080/00958972.2011.583646.

[13] D. Rai, L.E. Eary, J.M. Zachara, Environmental chemistry of chromium, Sci. Total Environ. 86 (1–2) (1989) 15–23, https://doi.org/10.1016/0048-9697(89)90189-7.

[14] L. Edmond Eary, Dhanpat Rai, Kinetics of Chromium(III) oxidation to Chromium (VI) by reaction with manganese dioxide, Environ. Sci. Technol. 21 (12) (1987) 1187–1193, https://doi.org/10.1021/es00165a005.

[15] Maurizio Pettine, Silvio Capri, Digestion treatments and risks of Cr(III)–Cr(VI) interconversions during Cr(VI) determination in soils and Sediments—A review, Anal. Chim. Acta 540 (2) (2005) 231–238, https://doi.org/10.1016/j.aca.2005.03.040.

[16] David C. Schroeder, G. Fred Lee, Potential transformations of chromium in natural waters, Water Air Soil Pollut. 4 (3–4) (1975) 355–365, https://doi.org/10.1007/BF00280721.

[17] Sandhya Mishra, Naresh Bharagava Ram, Toxic and genotoxic effects of hexavalent chromium in environment and its bioremediation strategies, J. Environ. Sci.Health, Part C 34 (1) (2016) 1–32, https://doi.org/10.1080/10590501.2015.1096883.

[18] C.R. Panda, K.K. Mishra, B.D. Nayak, D.S. Rao, B.B. Nayak, Release behaviour of chromium from Ferrochrome slag, Int. J. Environ. Technol. Manag. 15 (3/4/5/6) (2012) 261–274, https://doi.org/10.1504/IJETM.2012.049227.

[19] Johan J. Coetzee, Neetu Bansal, Evans M.N. Chirwa, Chromium in environment, its toxic effect from chromite-mining and ferrochrome industries, and its possible bioremediation, Expo. Health 12 (1) (2020) 51–62, https://doi.org/10.1007/s12403-018-0284-z.

[20] Juha Ylimaunu, Sandra van der Veen, Sheraz Neffati, Environmental Properties and Legal Status of Ferrochrome Slag, 2017.

[21] O. Sariyev, L. Tolymbekova, M. Dossekenov, et al., Analysis and chromium recovery from ferrochrome Waste (Stockpiled refined Ferrochrome slags), Metals 15 (7) (2025) 740, https://doi.org/10.3390/met15070740.

[22] O. Sariyev, B. Kelamanov, M. Dossekenov, et al., Environmental characterization of ferrochromium production waste (Refined slag) and its carbonization product, Heliyon 10 (9) (2024) e30789, https://doi.org/10.1016/j.heliyon.2024.e30789.

[23] S. Mandina, T. Mugadza, Speciation of chromium in soils, plants and waste water at A ferrochrome slag dump in Gweru, IOSR J. Environ. Sci. Toxicol. Food Technol. 7 (4) (2013) 43–49, https://doi.org/10.9790/2402-0744349.

[24] Liesbeth Horckmans, Robert Möckel, Peter Nielsen, et al., Multi-Analytical characterization of slags to determine the chromium concentration for a possible Re-Extraction, Minerals 9 (10) (2019) 646, https://doi.org/10.3390/min9100646.

[25] A.M. Mirzayousef-Jadid, Schwerdtfeger Klaus, Redox equilibria of chromium in calcium silicate base melts, Metall. Mater. Trans. B 40 (4) (2009) 533–543, https://doi.org/10.1007/s11663-009-9225-3.

[26] Lijun Wang, Seshadri Seetharaman, Experimental studies on the oxidation states of chromium oxides in slag systems, Metall. Mater. Trans. B 41 (5) (2010) 946–954, https://doi.org/10.1007/s11663-010-9383-3.

[27] Deman Liu, Jiang Diao, Yiyu Qiu, Guang Wang, Gang Li, Bing Xie, Determination of chromium valence state in the CaO–SiO_2 –FeO–MgO–CrO *x System by X-Ray Photoelectron spectroscopy*, High Temp. Mater. Process. 39 (1) (2020) 351–356, https://doi.org/10.1515/htmp-2020-0036.

[28] James E. Penner-Hahn, X-Ray absorption spectroscopy in coordination chemistry, Coord. Chem. Rev. 190–192 (September) (1999) 1101–1123, https://doi.org/10.1016/S0010-8545(99)00160-5.

[29] J.J. Rehr, R.C. Albers, Theoretical approaches to X-Ray absorption fine structure, Rev. Mod. Phys. 72 (3) (2000) 621–654, https://doi.org/10.1103/RevModPhys.72.621.

[30] G.T. Seidler, D.R. Mortensen, A.J. Remesnik, et al., A laboratory-based hard x-Ray monochromator for high-resolution x-Ray emission spectroscopy and x-Ray absorption near edge structure measurements, Rev. Sci. Instrum. 85 (11) (2014) 113906, https://doi.org/10.1063/1.4901599.

[31] Zoltán Németh, Jakub Szlachetko, Éva G. Bajnóczi, György Vankó, Laboratory von Hámos X-Ray Spectroscopy for Routine Sample Characterization, Rev. Sci. Instrum. 87 (10) (2016) 103105, https://doi.org/10.1063/1.4964098.

[32] Wolfgang Malzer, Christopher Schlesiger, Birgit Kanngießer, A century of laboratory X-Ray absorption spectroscopy – a review and an optimistic outlook,

Spectrochim. Acta B Atom Spectrosc. 177 (March) (2021) 106101, https://doi.org/10.1016/j.sab.2021.106101.
[33] Rafał Fanselow, Michał Sobstel, Wojciech Błachucki, Jakub Szlachetko, Performance of a Laboratory von Hámos Type X-ray Spectrometer in X-ray Absorption Spectroscopy Study on 3d Group Metals, X Ray Spectrom. 52 (5) (2023) 247–253, https://doi.org/10.1002/xrs.3317.
[34] K. Klementiev, R. Chernikov, XAFSmass: a Program for calculating the optimal mass of XAFS samples, J. Phys. Conf. 712 (May) (2016) 012008, https://doi.org/10.1088/1742-6596/712/1/012008.
[35] Mark C. Biesinger, Brad P. Payne, Andrew P. Grosvenor, Leo W.M. Lau, Andrea R. Gerson, Roger St C. Smart, Resolving surface chemical states in XPS analysis of first row transition metals, oxides and hydroxides: cr, Mn, Fe, Co and Ni, Appl. Surf. Sci. 257 (7) (2011) 2717–2730, https://doi.org/10.1016/j.apsusc.2010.10.051.
[36] Moniek Tromp, Jerome Moulin, Gillian Reid, John Evans, Cr K-Edge XANES spectroscopy: ligand and oxidation state dependence — what is oxidation state? AIP Conf. Proc. 882 (2007) 699–701, https://doi.org/10.1063/1.2644637.
[37] Tami E. Westre, Pierre Kennepohl, Jane G. DeWitt, Britt Hedman, Keith O. Hodgson, Edward I. Solomon, A Multiplet Analysis of Fe K-Edge 1s F 3d Pre-edge Features of Iron Complexes, 1997.
[38] P. Glatzel, U. Bergmann, High resolution 1s Core hole X-Ray spectroscopy in 3d transition metal Complexes—Electronic and structural information, Coord. Chem. Rev. 249 (1–2) (2005) 65–95, https://doi.org/10.1016/j.ccr.2004.04.011.
[39] Frank E. Huggins, Mohammad Najih, Gerald P. Huffman, Direct Speciation of Chromium in Coal Combustion By-Products by X-Ray Absorption FIne-Structure Spectroscopy 78 (2) (1999), https://doi.org/10.1016/S0016-2361(98)00142-2.
[40] B. Ravel, M. Newville, Athena , ARTEMIS , hephaestus : data analysis for X-Ray absorption spectroscopy using IFEFFIT, J. Synchrotron Radiat. 12 (4) (2005) 537–541, https://doi.org/10.1107/S0909049505012719.
[41] Dogan Paktunc, Jason P. Coumans, David Carter, Nail Zagrtdenov, Dominique Duguay, Mechanism of the direct reduction of chromite process as a clean ferrochrome technology, ACS Eng. Au 4 (1) (2024) 125–138, https://doi.org/10.1021/acsengineeringau.3c00057.
[42] Facun Jiao, Niken Wijaya, Lian Zhang, Yoshihiko Ninomiya, Rosalie Hocking, Synchrotron-based XANES speciation of chromium in the oxy-fuel fly ash collected from lab-scale drop-tube furnace, Environ. Sci. Technol. 45 (15) (2011) 6640–6646, https://doi.org/10.1021/es200545e.
[43] A. Vaitkus, A. Merkys, T. Sander, et al., A workflow for deriving chemical entities from crystallographic data and its application to the crystallography open database, J. Cheminf. 15 (1) (2023) 123, https://doi.org/10.1186/s13321-023-00780-2.
[44] P. Fornasini, R. Grisenti, On EXAFS debye-waller factor and recent advances, J. Synchrotron Radiat. 22 (5) (2015) 1242–1257, https://doi.org/10.1107/S1600577515010759.